Study of a 6-Leg Floating Interleaved Boost Converter with Coupled Inductors for Fuel Cell Heavy-Duty Electric Vehicles

Niema EL HADDAJI[1], Abdesslem DJERDIR[1], Serge PIERFEDERICI[2], Daniel HISSEL[1,3]
[1]Université Marie et Louis Pasteur, UTBM, CNRS, Institut FEMTO-ST, FCLAB, Belfort, France
[2]Université de Lorraine, CNRS, LEMTA, Vandœuvre-Lès-Nancy, France
[3]Institut Universitaire de France (IUF), France
E-mails: niema.elhaddaji@femto-st.fr, abdesslem.djerdir@utbm.fr,
serge.pierfederici@univ-lorraine.fr, daniel.hissel@univ-fcomte.fr

ACKNOWLEDGMENT

This work was supported by the EIPHI Graduate School (Contract ANR-17-EURE-0002) and the Region Bourgogne Franche-Comté. The HYSySPEM project was funded by the "France 2030" government investment plan managed by the French National Research Agency, under the reference "ANR-22-PEHY-0018."

***Index Terms*—Fuel Cell, Hybrid Electric Vehicle, DC-DC Power Converter, Boost, Coupled Inductors.**

***Abstract*—The transition to sustainable transportation has positioned hydrogen fuel cells as a key solution for heavy-duty vehicles, offering high efficiency, sustained power output, and rapid refueling capabilities. DC-DC power converters play a crucial role in adapting the fuel cell's output voltage to meet vehicular requirements. This paper compares three converter topologies: the three-phase interleaved boost converter (3-IBC), its coupled-inductor version, and the six-leg floating interleaved boost converter with coupled inductors (FIBCCI-6L). MATLAB/Simulink simulations assess current ripple performance, highlighting trade-offs in efficiency and component size for heavy-duty fuel cell applications.**

I. INTRODUCTION

In light of escalating environmental imperatives and evolving regulatory frameworks, the transportation industry is at a pivotal juncture, as evidenced by the rapid transition from conventional diesel-powered vehicles to more sustainable alternatives such as battery-electric and hydrogen fuel cell vehicles [1].Fuel cell technology in heavy-duty vehicles excels in delivering sustained power output and operational efficiency, especially under significant loads and prolonged usage. The rapid refueling capabilities, comparable to those of diesel, minimize downtime, enhancing productivity across transportation sectors. These properties establish fuel cells as a superior choice for applications requiring extended range and reliability, aligning with stringent environmental regulations and efficiency mandates [2].Subsequent to the deployment of hydrogen fuel cell technology within heavy-duty transportation platforms, the critical role of DC-DC power converters emerges as a cornerstone for optimizing vehicular energy management systems. These power devices are indispensable for elevating the typically lower voltage output from fuel cells to meet the higher voltage requirements of the vehicle's electrical subsystems. Selecting the ideal DC-DC converter for fuel cell electric vehicles hinges on critical factors such as high efficiency, power density, reliability, affordability, and minimal current ripple. These factors are essential to enhance vehicle performance, prolong component durability, and ensure cost-effectiveness [3].

Numerous topologies of DC-DC converters have been employed in fuel cell electric vehicles, each tailored to meet specific performance and efficiency requirements. In [4], [5], [6], the authors have utilized interleaved boost converters (IBC). These present various advantages such as decreasing input current ripples, which is highly recommended when using a fuel cell [7].In these topologies, the precise determination of the number of phases is essential. Although increasing the number of phases effectively reduces current ripple, it also requires larger number of magnetic components, a significant drawback in transportation systems where minimizing size and weight is critical [5] Beyond the IBCs, the floating interleaved boost converter (FIBC) has been identified as an improvement, retaining all the advantages of the IBC while offering superior voltage gain [8]. To further improve efficiency and minimize the size of magnetic components [9], the structure was modified by incorporating coupled inductors (CI) in place of uncoupled inductors.

This paper provides a comparative analysis of 3-IBC in both its uncoupled and coupled (cascaded cyclic)

forms, as well as FIBCCI-6L, which serves as a direct enhancement of the previous models. This study explicitly focuses on their application within fuel cell systems, particularly in heavy-duty applications. Simulations were conducted in open-loop configuration using the SimPower Systems tool in MATLAB/Simulink to evaluate the performance of these three topologies. The comparison focuses on current ripple performance and fault tolerance across the different architectures.

II. Study and Modeling of the 3 Topologies of DC-DC Power Converters

A. The 3-IBC Topology

The topology is illustrated in Fig. 1 topology of IBC converter with its operating principle thoroughly explained in [10]. The primary components include switches S_1, S_2, S_3, diodes D_1, D_2, D_3, inductors L_1, L_2, L_3, and an output smoothing capacitor C. The load resistance is represented by R, the input voltage by V_{fc}, and the output voltage by V_o. Each phase operates

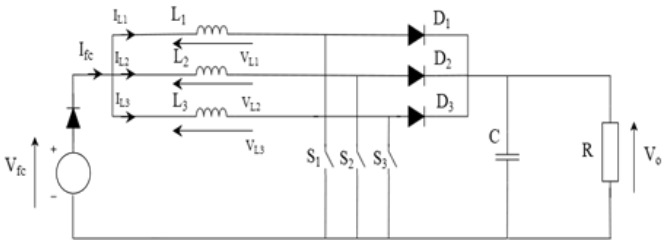

Fig. 1. 3-IBC

with the same duty ratio d and a phase shift of 120° between them. The voltage expressions for this topology are expressed in (1).

$$\begin{bmatrix} V_{L1} \\ V_{L2} \\ V_{L3} \end{bmatrix} = \begin{bmatrix} L_1 & 0 & 0 \\ 0 & L_2 & 0 \\ 0 & 0 & L_3 \end{bmatrix} \frac{d}{dt} \begin{bmatrix} i_{L1} \\ i_{L2} \\ i_{L3} \end{bmatrix}. \quad (1)$$

B. The 3-IBC Topology with CI

There are various coupling structures available for multiphase converters. The cascade cyclic structure was chosen among them because it is more compact than other configurations that require a large number of transformers, such as the combinatorial cascade structure [11]. This design is also simpler to implement, as it can be assembled using standard cores. Furthermore, using separate transformers is beneficial in the event of a failure, as any saturation will be localized to the specific affected phases.

The Fig. 2 presents a 3-IBC with cascade cyclic CIs. It includes the same components as mentioned for Fig. 1

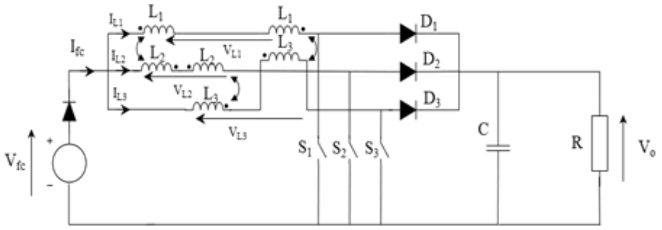

Fig. 2. 3-IBC CI

but differs in the inductor configuration. Each inductor is divided into two parts, where the first part of L_1 is coupled with the first part of L_2, the second part of L_2 with the first part of L_3, and finally the second part of L_3 is coupled with the second part of L_1, giving rise to what is called a cyclic cascade configuration. The coupling between each pair of inductors is an inverse-coupled configuration. This configuration ensures the cancellation of the DC fluxes, which are generated according to the average currents in the inductors. Additionally, it reduces the ripple currents in the inductors [12]. The voltage equations for this topology are given in (2).

$$\begin{bmatrix} V_{L1} \\ V_{L2} \\ V_{L3} \end{bmatrix} = \begin{bmatrix} 2L_1 & -M_{21} & -M_{31} \\ -M_{12} & 2L_2 & -M_{32} \\ -M_{13} & -M_{23} & 2L_3 \end{bmatrix} \frac{d}{dt} \begin{bmatrix} i_{L1} \\ i_{L2} \\ i_{L3} \end{bmatrix}. \quad (2)$$

M represents the mutual inductance and is preceded by a minus sign (-), indicating inverse coupling. The coupling coefficient is given by $k = \frac{M}{L}$.

C. The FIBCCI-6L Topology

The topology shown in Fig. 3 presents the proposed FIBCCI-6L. It is composed of two modular sections: the upper section is a non-floating version of the 3-IBC, while the lower section is a floating version of the 3-IBC. To maintain equilibrium between the top floating module and the bottom non-floating module, the number of phases must be paired.

This topology is characterized by a floating output and an interleaved input, which effectively reduces both current and voltage stress. The operating principle of the 2-leg floating boost converter is thoroughly explained in [8]. By analogy, the same operating principle applies to the 6-leg Floating Interleaved Boost Converter, except that in this case, the phase shift is 60°. The voltage

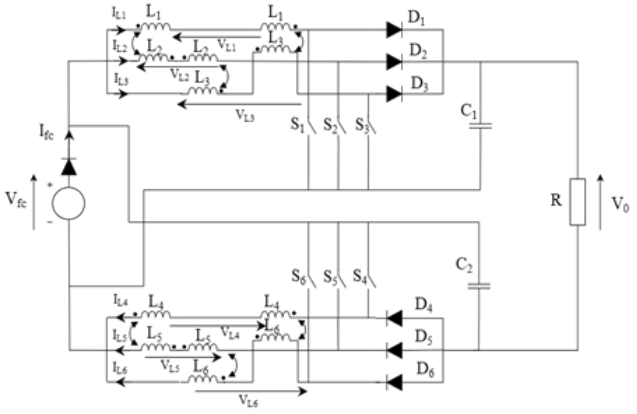

Fig. 3. FIBCCI-6L

expressions in this case are defined in (3)

$$\begin{bmatrix} V_{L1} \\ V_{L2} \\ V_{L3} \\ V_{L4} \\ V_{L5} \\ V_{L6} \end{bmatrix} = \begin{bmatrix} A & 0 \\ 0 & B \end{bmatrix} \frac{d}{dt} \begin{bmatrix} i_{L1} \\ i_{L2} \\ i_{L3} \\ i_{L4} \\ i_{L5} \\ i_{L6} \end{bmatrix}. \tag{3}$$

Where

$$A = \begin{bmatrix} 2L_1 & -M_{21} & -M_{31} \\ -M_{12} & 2L_2 & -M_{32} \\ -M_{13} & -M_{23} & 2L_3 \end{bmatrix} \tag{4}$$

$$B = \begin{bmatrix} 2L_4 & -M_{54} & -M_{64} \\ -M_{45} & 2L_5 & -M_{65} \\ -M_{46} & -M_{56} & 2L_6 \end{bmatrix} \tag{5}$$

III. Analysis of the 3-IBC with CI

The three switches in Fig. 2 operate under the same duty cycle, each phase-shifted by $T_s/3$. Across all duty cycle ranges, there are eight operational modes, according to the ON/OFF state of the power switches, shown in Table I.

According to Kirchhoff's law, when the main switches are in the on-state, the voltage across the inductor winding equals the input voltage. Conversely, in the off-state, this voltage is determined by the difference between the input and output voltages in (6)

$$\begin{aligned} V_{L_{\text{on}}} &= V_{\text{Fc}} \\ V_{L_{\text{off}}} &= V_{\text{FC}} - V_o \end{aligned} \tag{6}$$

To ensure system balance and symmetry of the magnetic core, $L_1 = L_2 = L_3 = L$ and $M_{12} = M_{21} = M_{23} = M_{32} = M_{13} = M_{31} = M$.

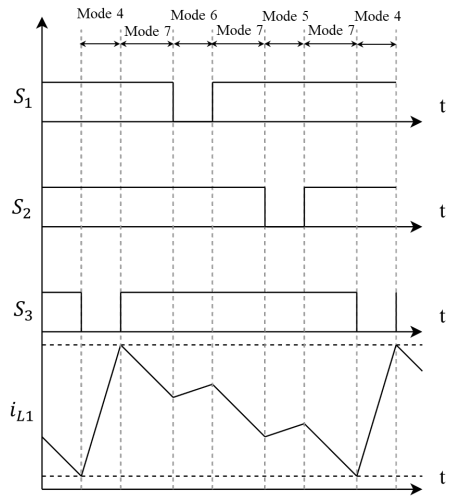

(a) Duty ratio $<$ 1/3

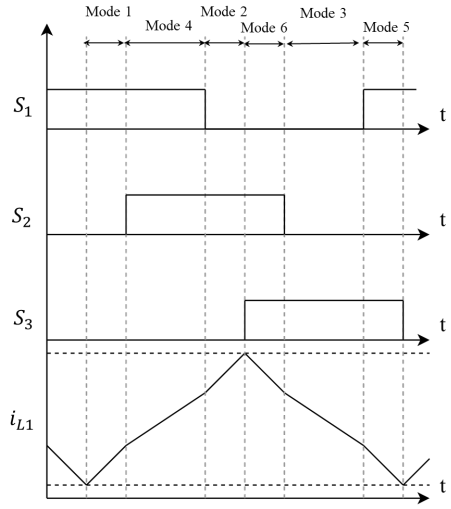

(b) $1/3 <$ Duty ratio $\leq 2/3$

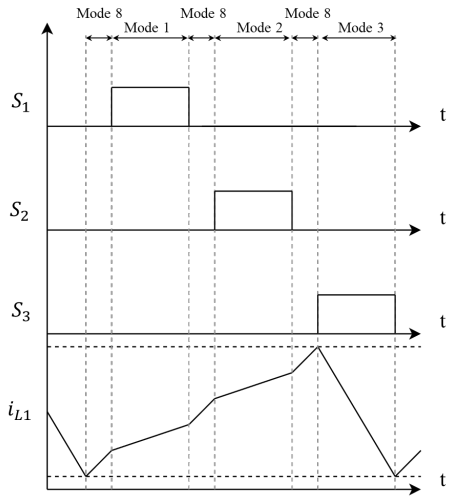

(c) Duty ratio $>$ 2/3

Fig. 4. Inductor current waveforms for phase 1 across the full range of duty ratios.

TABLE I Operational Modes

Mode	S1	S2	S3
Mode 1	ON	OFF	OFF
Mode 2	OFF	ON	OFF
Mode 3	OFF	OFF	ON
Mode 4	ON	OFF	OFF
Mode 5	ON	OFF	ON
Mode 6	OFF	ON	ON
Mode 7	ON	ON	ON
Mode 8	OFF	OFF	OFF

$$\begin{cases} \frac{di_{L1}}{dt} = \frac{(2L-M)V_{L1}+MV_{L2}+MV_{L3}}{4L^2-2LM-2M^2}, \\ \frac{di_{L2}}{dt} = \frac{MV_{L1}+(2L-M)V_{L2}+MV_{L3}}{4L^2-2LM-2M^2}, \\ \frac{di_{L3}}{dt} = \frac{MV_{L1}+MV_{L2}+(2L-M)V_{L3}}{4L^2-2LM-2M^2}. \end{cases} \tag{7}$$

Based on (7), the time derivative of the inductor currents can be expressed as follows:

Throughout the first operation mode (Mode 1), the switch S_1 is ON and the switches S_2 and S_3 are OFF, which means

$$V_{L1} = V_{FC} \tag{8}$$

$$V_{L2} = V_{L3} = V_{FC} - V_o \tag{9}$$

From (7), the derivative of the inductor current in the first phase can be expressed as

$$\frac{di_{L1}(t)}{dt} = \frac{M - 2L + 2Ld + Md}{2(d-1)(-2L^2 + LM + M^2)} V_{L1} \tag{10}$$

Knowing that,

$$V_{L1} = L_{\text{eq1}} \frac{di_{L1}}{dt} \tag{11}$$

From (10), L_{eq1} can be written as below

$$L_{\text{eq1}} = \frac{2(d-1)(-2L^2 + LM + M^2)}{M - 2L + 2Ld + Md} \tag{12}$$

Using the same method, the equivalent inductance for phase 1 in other modes can be obtained as follows

Mode 2

$$L_{\text{eq2}} = \frac{2d(-2L^2 + LM + M^2)}{2Ld - M + Md} \tag{13}$$

Mode 3

$$L_{\text{eq3}} = \frac{2d(-2L^2 + LM + M^2)}{2Ld - M + Md} \tag{14}$$

Mode 4

$$L_{\text{eq4}} = \frac{2(d-1)(-2L^2 + LM + M^2)}{2Ld - 2L + Md} \tag{15}$$

Mode 5

$$L_{\text{eq5}} = \frac{2d(-2L^2 + 2M + M^2)}{2Ld - 2L + Md} \tag{16}$$

Mode 6

$$L_{\text{eq6}} = \frac{2d(-2L^2 + LM + M^2)}{2Ld - 2M + Md} \tag{17}$$

Mode 7

$$L_{\text{eq7}} = 2(L - M) \tag{18}$$

Mode 8

$$L_{\text{eq8}} = 2(L - M) \tag{19}$$

The differential values of inductance L across distinct operating modes of the converter are the primary determinants of the observed variations in the slopes of the current waveform. For each duty ratio, equivalent inductances can be expressed as a function of operating modes.

- Duty ratio $> \frac{1}{3}$
  As shown in Fig. 4a, there are 4 operation modes. The transition between these modes occurs in the sequence of modes 4, 7, 6, 7.5, and 7.
- $\frac{1}{3} <$ Duty ratio $\leq \frac{2}{3}$
  In this instance, Fig. 4b, the operation modes transition through modes 1, 4, 2, 6, 3, and 5.
- Duty ratio $> \frac{2}{3}$
  In this case, Fig. 4c, the operation modes shift between modes 8, 1, 8, 2, 8, and 3.

Fig. 4 presents the current waveform of the first phase across different duty ratio ranges. The equivalent inductances of phases 2 and 3 for each duty ratio can be determined following the same steps.

Similarly, for the FIBCCI-L6 (Fig. 3), the analysis builds upon that of the 3-IBC with CI. This is justified as the FIBCCI-L6 essentially consists of two 3-IBC CI modules, where the three inductors in the non-floating section operate independently of the floating section, maintaining behavior consistent with the 3-IBC CI.

A key aspect that differs in this analysis is the ideal voltage gain, defined by Eq. (20), which applies specifically to the Floating Interleaved Boost Converter:

$$M(D) = \frac{V_o}{V_{\text{in}}} = \frac{1+D}{1-D}. \tag{20}$$

As previously indicated, the FIBC exhibits a superior voltage gain relative to both the coupled and uncoupled versions of the IBC. This assertion is substantiated by Fig. 5, which clearly demonstrates the comparative performance metrics.

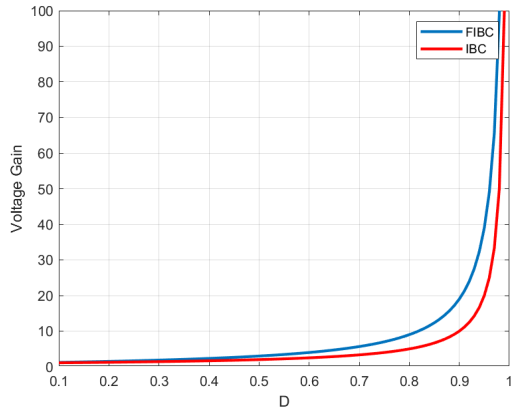

Fig. 5. Comparative performance metrics of IBC and FIBC.

IV. Numerical Simulation and Comparison of the Behavior of the Proposed Topologies

Numerical simulations were performed in MATLAB/Simulink to evaluate and compare the performance of three topologies: the 3-IBC as the baseline, the 3-IBC with CIs as the first enhancement, and the FIBCCI-6L as the second enhancement. Initially, the converters operated under standard conditions. To assess fault tolerance, an open-circuit fault was simulated in phase 1.

This type of fault is particularly critical in hydrogen fuel cell systems [13] , where consistent and reliable power delivery is essential. Such faults disrupt electrical flow, potentially causing voltage fluctuations that compromise fuel cell efficiency and reliability. This is especially crucial in applications requiring an uninterrupted power supply, such as electric vehicles. The rated parameters of the converters are listed in Table II.

TABLE II Converters Rated Parameters

Parameters	**Value**	**Unit**
Output Voltage (V_o)	800	V
Input Voltage (V_{fc})	176	V
Switching Frequency (f_s)	80	kHz
Inductor (L, r_L)	(122, 0.2)	(μH, mΩ)
Capacity (C)	80	μF
Coupling Coefficient (k)	0.3	-
Tolerated Output Voltage Ripple (ΔV_o)	$\leq$10%	-
Tolerated Input Current Ripple (ΔI_{fc})	$\leq$10%	-
Duty Ratio (IBC, FIBC)	(0.75, 0.63)	-

The integration of coupled inductors not only contributes to the reduction in the size of magnetic components, - the decrease in the size of the magnetic component is indicated by the reduction in the amount of energy stored in inductors across the three topologies, as shown on Fig. 7 and improves overall efficiency, but

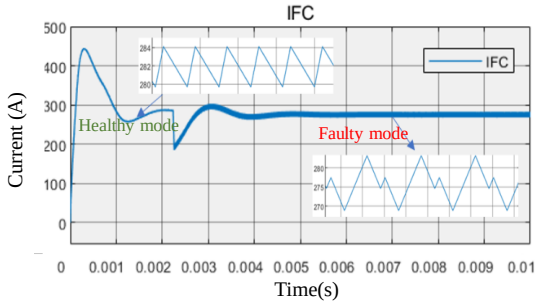

(a) 3-IBC Healthy and Faulty Mode

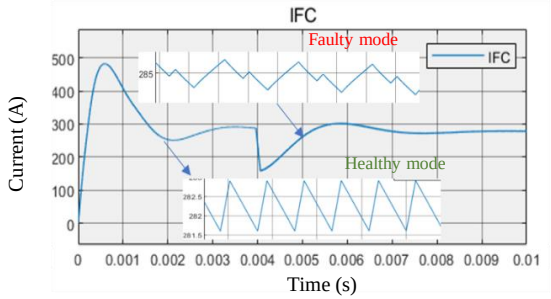

(b) 3-IBC CI Healthy and Faulty Mode

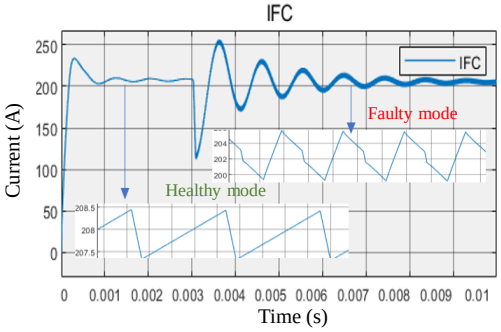

(c) FIBCCI-6L Healthy and Faulty Mode

Fig. 6. Fuel cell Current waveform

also demonstrates superior fault tolerance compared to the reference structure.

In the healthy operating mode, the variation in input current ripple, as depicted in Fig. 6, is relatively minor across the three configurations. However, a significant distinction emerges when examining the inductor current ripple, as illustrated in Fig. 9

Notably, a 63.98% reduction in current ripple was achieved with the use of the FIBCCI-6L. This difference is particularly pronounced under faulty conditions. Among the topologies evaluated, the reference converter exhibited the least favorable performance metrics. In

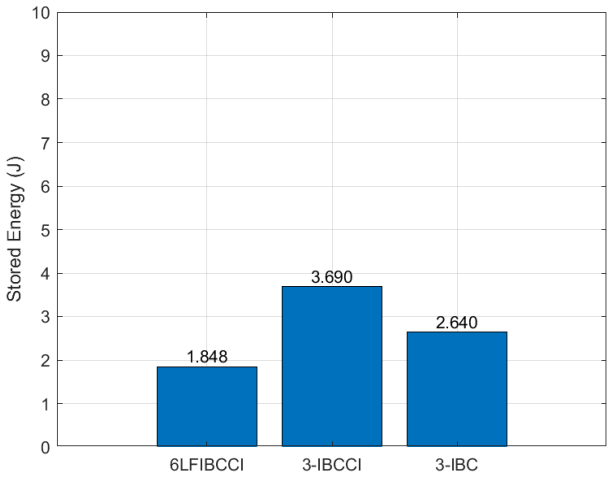

Fig. 7. Comparative of the stored energies in the proposed topologies

contrast, the two converters incorporating coupled inductors outperformed the reference, with only a slight difference observed between them.

The detailed values depicted in the waveform graphs are explicitly outlined in Table III, further validating the effectiveness of coupled inductors in mitigating current ripple, especially under fault conditions, thereby strengthening the overall robustness of the converter system.

TABLE III Performance Metrics in Different Modes

(a) Healthy Mode

	3-IBC	**3-IBC CI**	**FIBCCI-6L**
ΔI_{fc} (A)	4.43	3.11	1.12
ΔI_L (A)	13.35	6.18	4.81
ΔI_{out} (A)	0.09	0.09	0.0592

(b) Faulty Mode

	3-IBC	**3-IBC CI**	**FIBCCI-6L**
ΔI_{fc} (A)	14.54	8.85	6.14
ΔI_L (A)	12.77	6.21	5.20
ΔI_{out} (A)	0.4	0.4	0.4

Additionally, it is important to highlight that the variation in the output current Fig. 8 remains negligible in both healthy and faulty modes, reinforcing the consistency and robustness of the output current across all configurations. Furthermore, the presence of a nonzero current at $t = 0s$ is due to the initial condition on the capacitors voltage, set at $V_{C0} = 400V$.

When a fault occurred in the first set of inductors (non-floating module) within the FIBCCI-6L configuration, the second set of inductors (floating module)

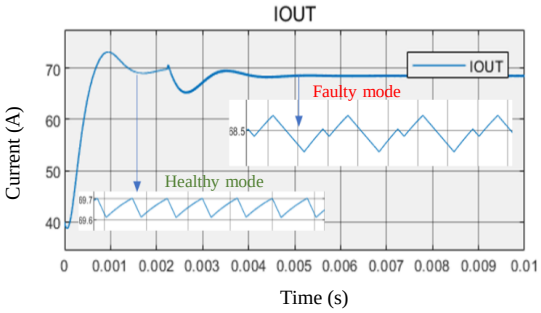

(a) 3-IBC Healthy and Faulty Mode

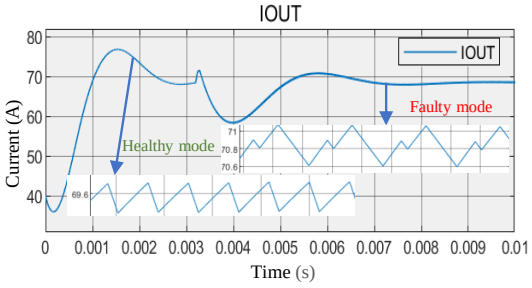

(b) 3-IBC CI Healthy and Faulty Mode

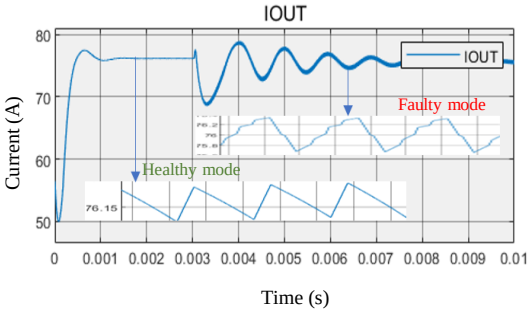

(c) FIBCCI-6L Healthy and Faulty Mode

Fig. 8. Output Current waveform

remained unaffected. This observation -as shown in Fig. 9c- underscores the independent operation of the two modules, a feature attributed to the modular design of the system, which employs a mirror-effect principle to balance currents between the floating and non-floating components. However, the introduction of a fault in the non-floating module disrupted this balance, as the fault was not mirrored in the floating module, resulting in a transient current imbalance.

To address this, a deliberate fault was introduced in a phase of the floating module at 0.005s. As illustrated in the Fig. 10, this intervention enabled a partial restoration of the current balance between the two modules. To fur-

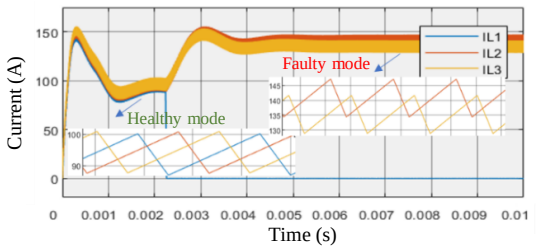

(a) 3-IBC Healthy and Faulty Mode

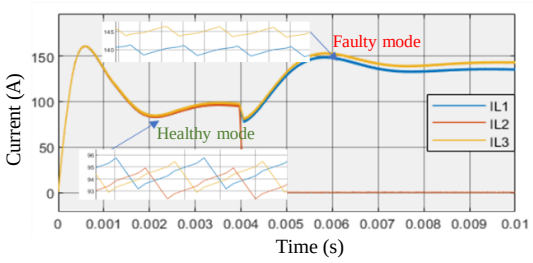

(b) 3-IBC CI Healthy and Faulty Mode

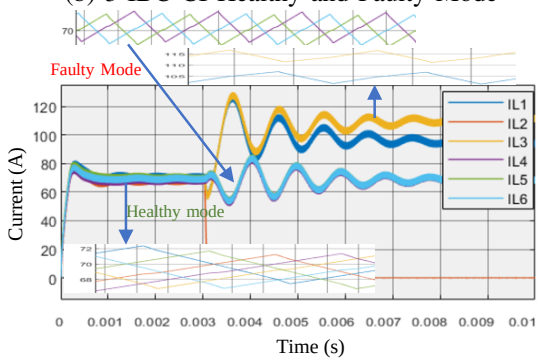

(c) FIBCCI-6L Healthy and Faulty Mode (1 Fault)

Fig. 9. Inductors Current waveform for different fault scenarios

ther validate this behavior, the simulation was extended to include the impact of a second fault. This extension provided additional insight into the system's fault-tolerant behavior, demonstrating that the currents tend to rebalance even under compounded fault conditions.

By redistributing the current flow, the system demonstrated its inherent self-regulating capability to adapt and maintain operational stability under fault conditions. Despite the transient imbalance caused by the initial fault, the overall system performance remained unaffected. This robustness and fault-tolerant design of the FIBCCI-6L configuration highlights its ability to maintain consistent performance under fault scenarios, making it a reliable solution for applications that demand high stability and resilience.

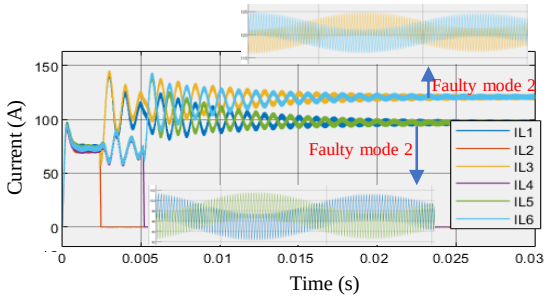

Fig. 10. FIBCCI-6L Healthy and Faulty Mode (2 Faults)

V. Conclusion

The results clearly indicate that the 3-IBC is surpassed in performance by the two proposed topologies. Although the performance metrics of the two new converters are relatively close, the FIBCCI-6L exhibits a marginally better performance than the 3-IBC CI. This improvement substantiates the selection of this particular structure as the most optimal choice. Furthermore, this preference is reinforced by the long-term vision of integrating an energy storage system within the same converter framework, which is particularly feasible with the selected topology. Additionally, the experimental validation and control implementation of these structures are planned as part of future work to further confirm and optimize their performance.

References

[1] A. F. Burke, J. Zhao, M. R. Miller, A. Sinha, and L. M. Fulton, "Projections of the costs of medium- and heavy-duty battery-electric and fuel cell vehicles (2020-2040) and related economic issues," *Energy for Sustainable Development*, 2023. [Online]. Available: https://api.semanticscholar.org/CorpusID:265435039

[2] S. Pardhi, S. Chakraborty, D.-D. Tran, M. E. Baghdadi, S. S. Wilkins, and O. Hegazy, "A review of fuel cell powertrains for long-haul heavy-duty vehicles: Technology, hydrogen, energy and thermal management solutions," *Energies*, 2022. [Online]. Available: https://api.semanticscholar.org/CorpusID:254907383

[3] D. Guilbert, "Dimensionnement des composants magnétiques d'un convertisseur dc/dc boost entrelacé tolérant aux défauts pour des applications véhicule électrique à pile à combustible," 2014. [Online]. Available: https://api.semanticscholar.org/CorpusID:172049704

[4] A. V. Deshpande, B. K. Patil, R. B. Magadum, and N. R. Chitragar, "Design and simulation of interleaved boost converter," *2021 International Conference on System, Computation, Automation and Networking (ICSCAN)*, pp. 1–5, 2021. [Online]. Available: https://api.semanticscholar.org/CorpusID:237445998

[5] D. Guilbert, "Tolérance aux défauts et optimisation des convertisseurs DC/DC pour véhicules électriques à pile à combustible," Theses, Université de Technologie de Belfort-Montbeliard, Dec. 2014. [Online]. Available: https://theses.hal.science/tel-01499562

[6] H. Wang, "Design and control of a 6-phase interleaved boost converter based on sic semiconductors with eis functionality for fuel cell electric vehicle," 2019. [Online]. Available: https://api.semanticscholar.org/CorpusID:199153958

[7] Y. Gürlek, O. Joos, C. Lang, M. Ackerl, R. Dold, T. Basler, and M. Neuburger, "Analysis on the impact of current ripples in fuel cell electric heavy-duty trucks," in *2023 25th European Conference on Power Electronics and Applications (EPE'23 ECCE Europe)*. IEEE, 2023, pp. 1–8.

[8] S. Zhuo, A. Gaillard, D. Paire, E. Breaz, and F. Gao, "Design and control of a floating interleaved boost dc-dc converter for fuel cell applications," in *IECON 2018-44th Annual Conference of the IEEE Industrial Electronics Society*. IEEE, 2018, pp. 2026–2031.

[9] A. Paul, B. S. Ram, and S. Kulkarni, "Review of coupled inductors in power electronics: From concept to practice," *e-Prime-Advances in Electrical Engineering, Electronics and Energy*, p. 100501, 2024.

[10] M. A. Harimon, A. Ponniran, A. N. Kasiran, and H. H. Hamzah, "A study on 3-phase interleaved dc-dc boost converter structure and operation for input current stress reduction," *International Journal of Power Electronics and Drive Systems (IJPEDS)*, vol. 8, pp. 1948–1953, 2017. [Online]. Available: https://api.semanticscholar.org/CorpusID:116699524

[11] M. Benzine, I. Salhi, A. Gaillard, and F. Gao, "Coupled inductors-based interleaved boost converters for fuel cell electric vehicles," in *2023 IEEE Transportation Electrification Conference & Expo (ITEC)*. IEEE, 2023, pp. 1–7.

[12] J. Imaoka, M. Yamamoto, and T. Kawashima, "High-power-density three-phase interleaved boost converter with a novel coupled inductor," *IEEJ Journal of Industry Applications*, vol. 4, no. 1, pp. 20–30, 2015.

[13] D. Guilbert, A. N'Diaye, A. Gaillard, and A. Djerdir, "Fuel cell systems reliability and availability enhancement by developing a fast and efficient power switch open-circuit fault detection algorithm in interleaved dc/dc boost converter topologies," *International Journal of Hydrogen Energy*, vol. 41, no. 34, pp. 15 505–15 517, 2016.